Supplementary information

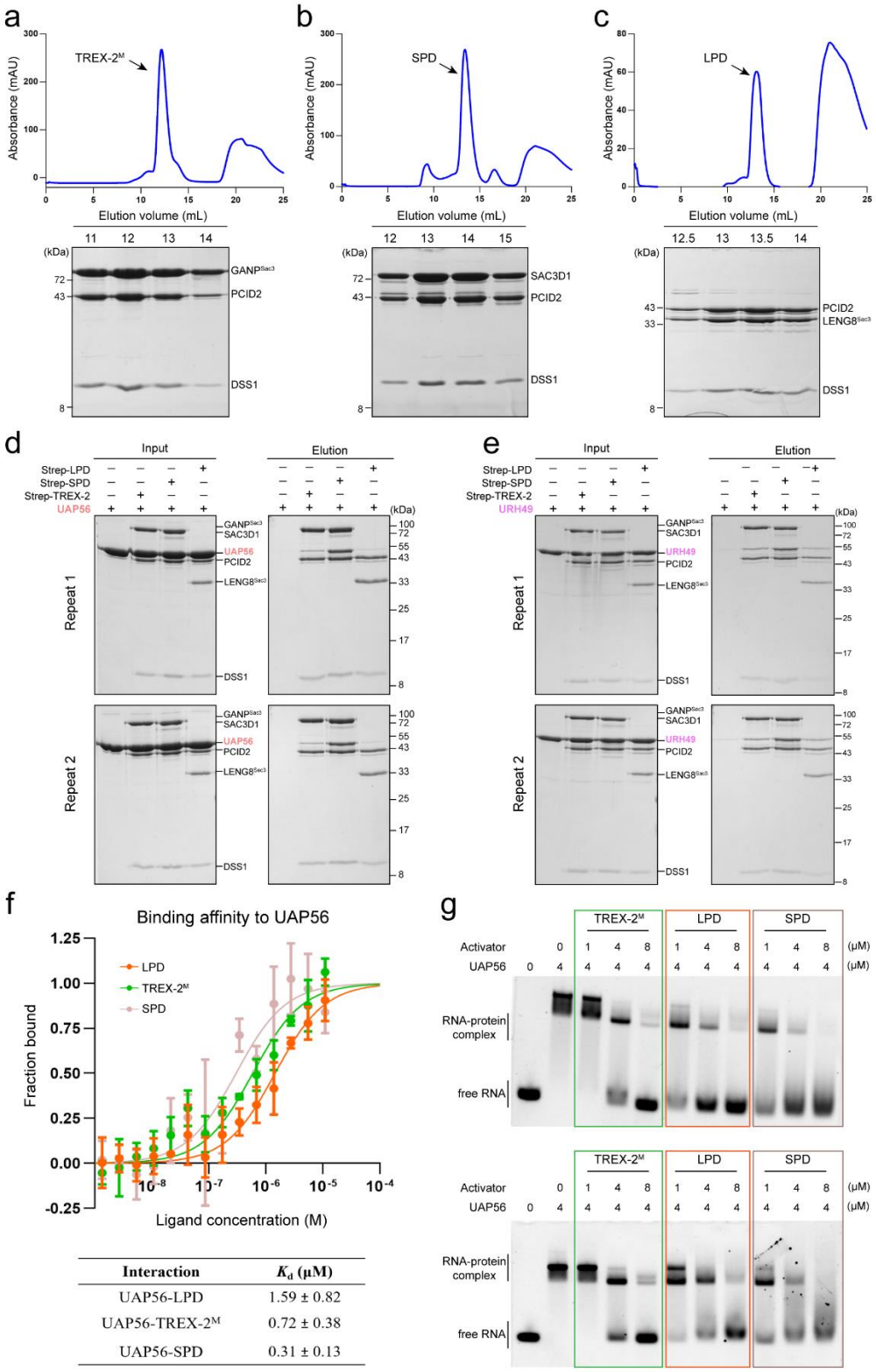

Interaction	K_d (μM)
UAP56-LPD	1.59 ± 0.82
UAP56-TREX-2^M	0.72 ± 0.38
UAP56-SPD	0.31 ± 0.13

Supplementary Fig. 1 | Biochemical characterization of TREX-2-like complexes

a-c, Size-exclusion chromatography (SEC) profiles and Coomassie blue-stained SDS-PAGE analyses of purified TREX-2^M (**a**), SPD (**b**), and LPD (**c**). The constituent

subunits are labeled. **d**, Two independent Strep-affinity pulldown assays examining the interactions of UAP56 with LPD, SPD, and TREX-2^{M}. Input and elution fractions were analyzed by SDS-PAGE. **e**, Two independent Strep-affinity pulldown assays examining the interactions of URH49 with LPD, SPD, and TREX-2^{M}. **f**, Binding affinities of LPD, TREX-2^{M}, and SPD for GFP-UAP56 measured by microscale thermophoresis. Data are presented as mean ± s.d. from three independent experiments. Solid lines represent fits to an equilibrium binding model. The resulting dissociation constants (K_d) are summarized below the graph. **g,** Two independent native electrophoretic mobility shift assays showing concentration-dependent RNA release from preassembled UAP56-RNA complexes following the addition of TREX-2^{M}, LPD, or SPD. Protein concentrations are indicated above the lanes.

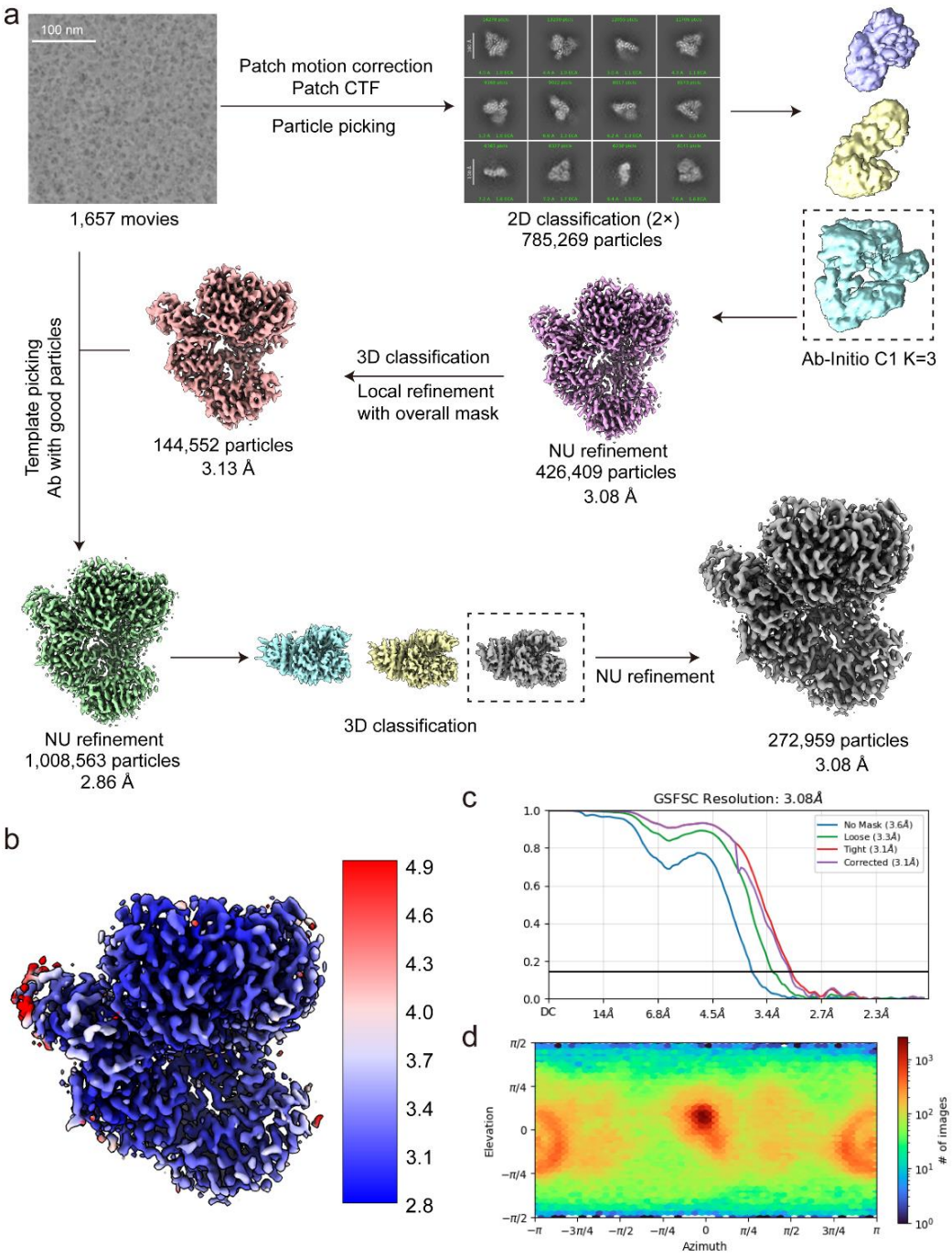

Supplementary Fig. 2 | Cryo-EM analysis of the UAP56-SPD complex

a, CryoSPARC processing workflow for the UAP56-SPD dataset. The number of particles and resolution of the indicated reconstruction are provided. **b**, Final cryo-EM map of the UAP56-SPD complex colored according to local resolution. **c**, Gold-standard Fourier shell correlation curves for the final UAP56-SPD reconstruction. The horizontal line indicates the FSC = 0.143 criterion. **d**, Angular distribution of the particles contributing to the final reconstruction.

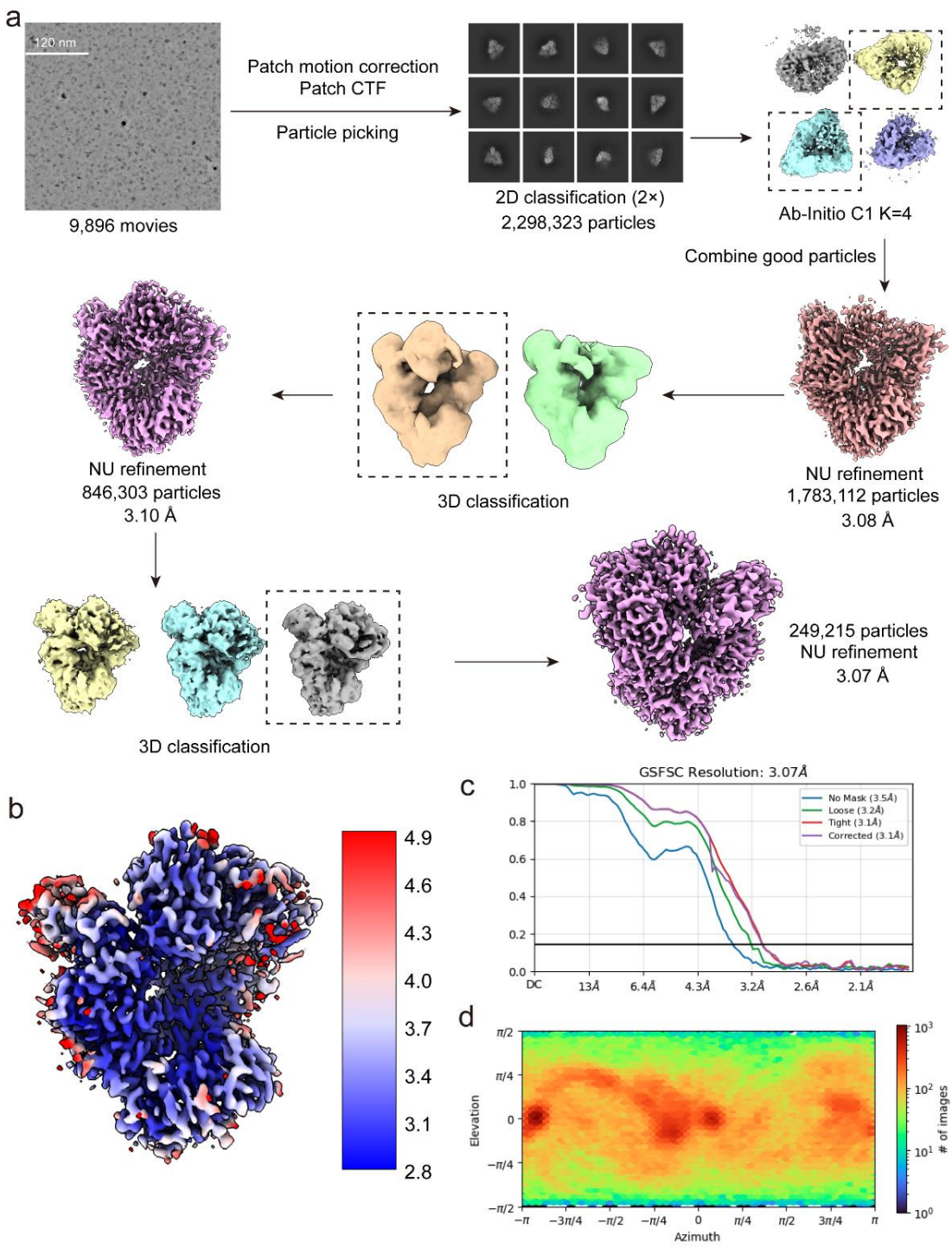

Supplementary Fig. 3 | Cryo-EM analysis of the URH49-SPD complex

a, CryoSPARC processing workflow for the URH49-SPD dataset. The number of particles and resolution of the indicated reconstruction are provided. **b**, Final cryo-EM map of the URH49-SPD complex colored according to local resolution. **c**, The final reconstruction has an average resolution of 3.07 Å as determined by the FSC value of 0.143. **d**, Angular distribution of the particles contributing to the final reconstruction.

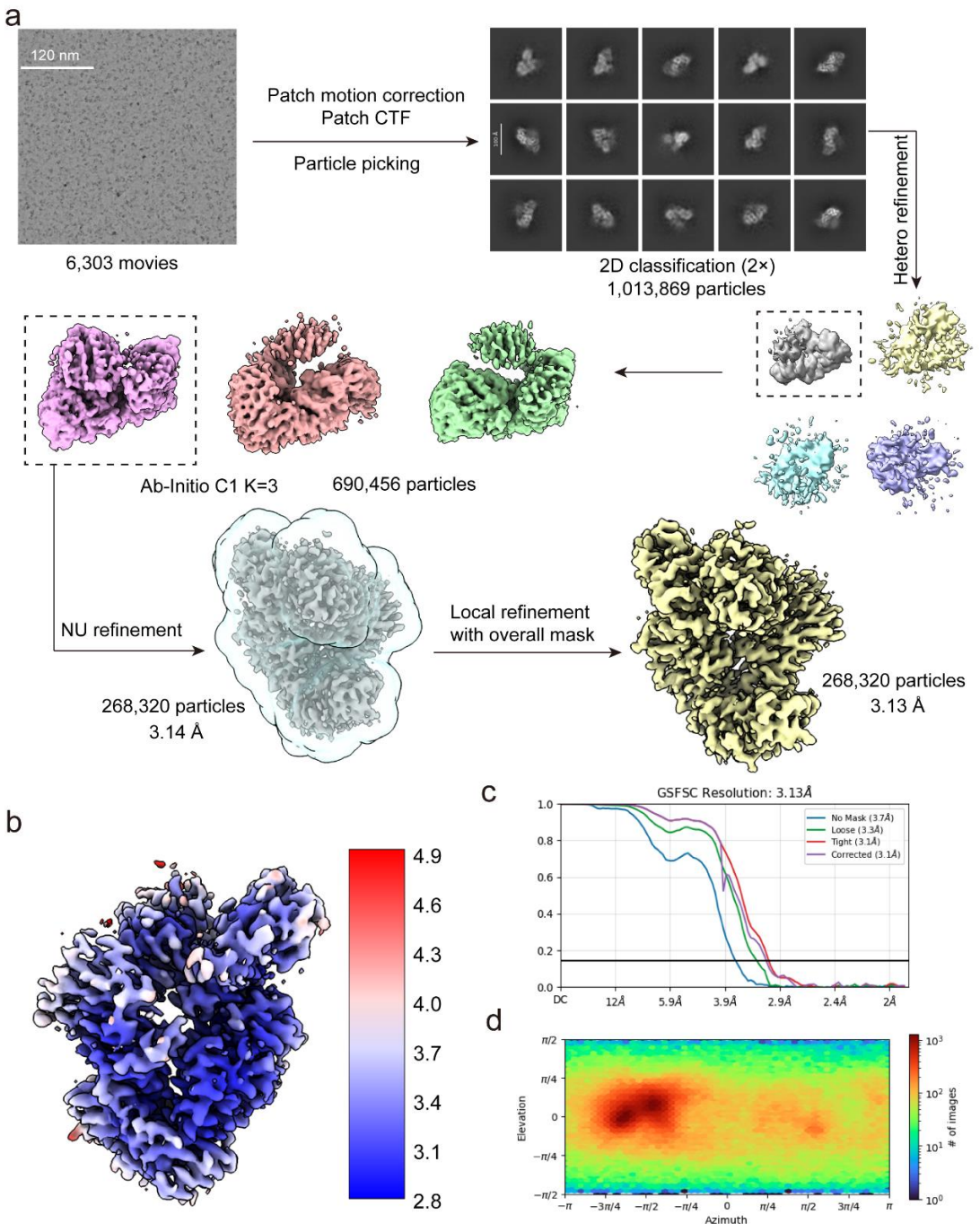

Supplementary Fig. 4 | Cryo-EM analysis of the UAP56-LPD complex

a, CryoSPARC processing workflow for the UAP56-LPD dataset. The number of particles and resolution of the indicated reconstruction are provided. **b**, Final cryo-EM map of the UAP56-LPD complex colored according to local resolution. **c**, Gold-standard Fourier shell correlation curves for the final UAP56-LPD reconstruction. The horizontal line indicates the FSC = 0.143 criterion. **d**, Angular distribution of the particles contributing to the final reconstruction.

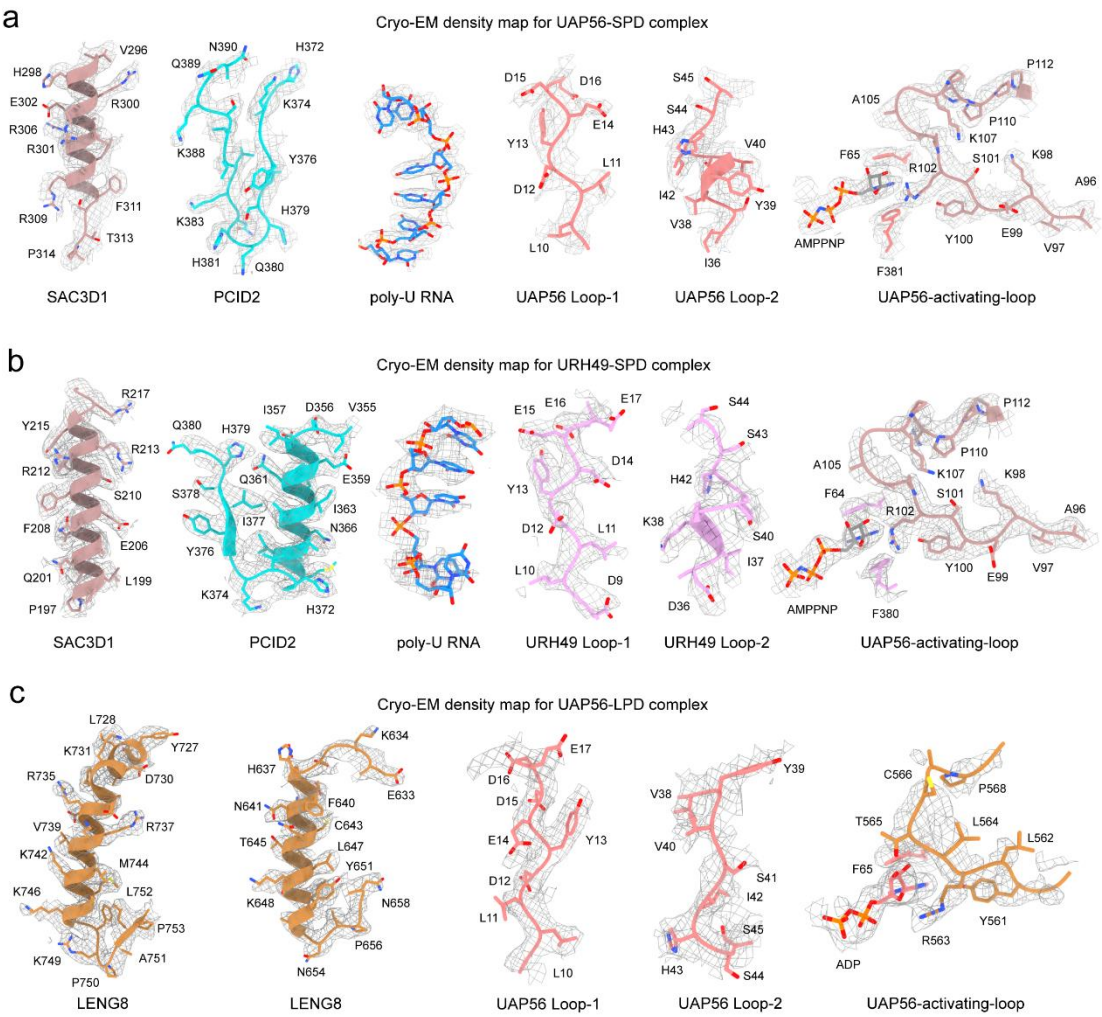

Supplementary Fig. 5 | Representative local cryo-EM densities for atomic model building

a, Representative cryo-EM densities and fitted atomic models for selected regions of the UAP56-SPD complex, including SAC3D1, PCID2, poly(U) RNA, UAP56 Loop-1, UAP56 Loop-2, and the activating-loop together with bound nucleotide. **b**, Representative cryo-EM densities and fitted atomic models for selected regions of the URH49-SPD complex. **c**, Representative cryo-EM densities and fitted atomic models for selected regions of the UAP56-LPD complex. Cryo-EM densities are shown as gray meshes.

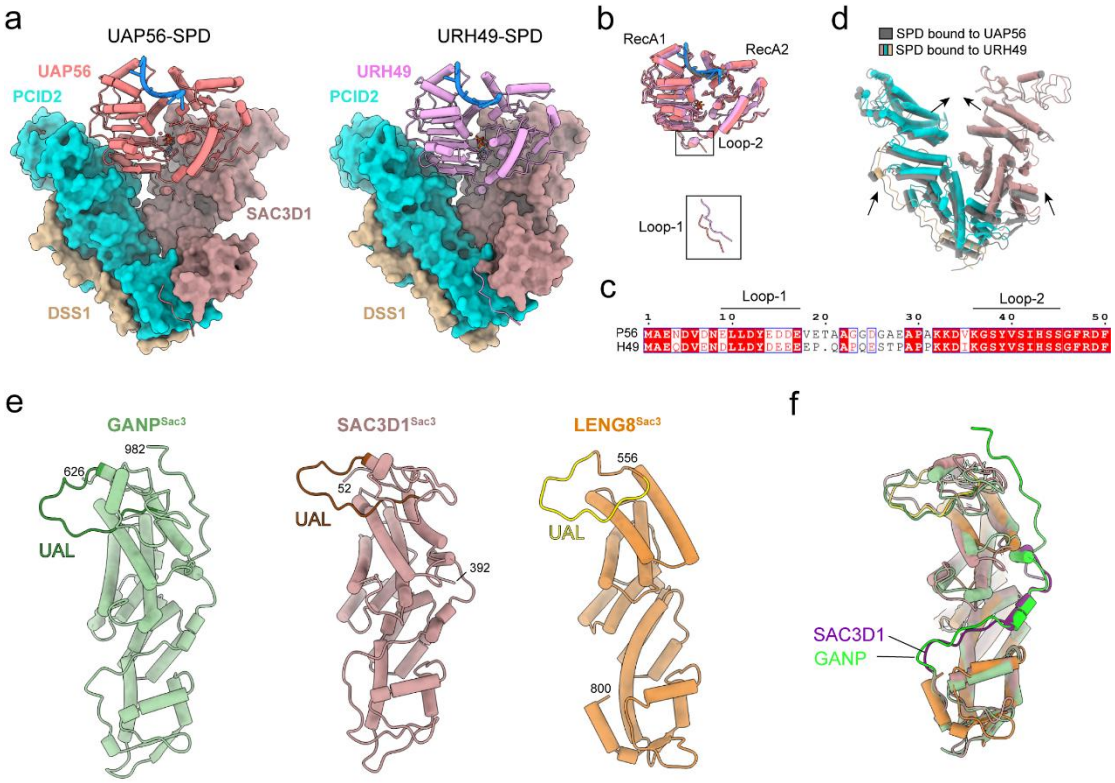

Supplementary Fig. 6 | Structural comparison of UAP56/URH49 and Sac3-family complexes

a, Overall structures of the UAP56-SPD and URH49-SPD complexes shown in the same orientation. Individual components are colored as indicated. UAP56 and URH49 are anchored on the surface of SPD. **b**, Structural superposition of UAP56 and URH49 in the SPD-bound complexes. Insets highlight the conformations of Loop-1 and Loop-2. **c**, Sequence alignment of the N-terminal regions of UAP56 and URH49. Segments corresponding to Loop-1 and Loop-2 are indicated. **d**, Structural superposition of SPD in the UAP56-bound and URH49-bound complexes. Arrows indicate regions that adopt different conformations in the two structures. **e**, Structures of the Sac3 domains of GANP, SAC3D1, and LENG8. The UAP56-activating loop is highlighted, and the modeled residue boundaries are indicated. **f**, Superposition of the Sac3 domains of GANP, SAC3D1, and LENG8, revealing a conserved core architecture and conformational differences in peripheral loops. SAC3D1 and GANP contains an additional C-terminal extension, colored magenta and lime, respectively.

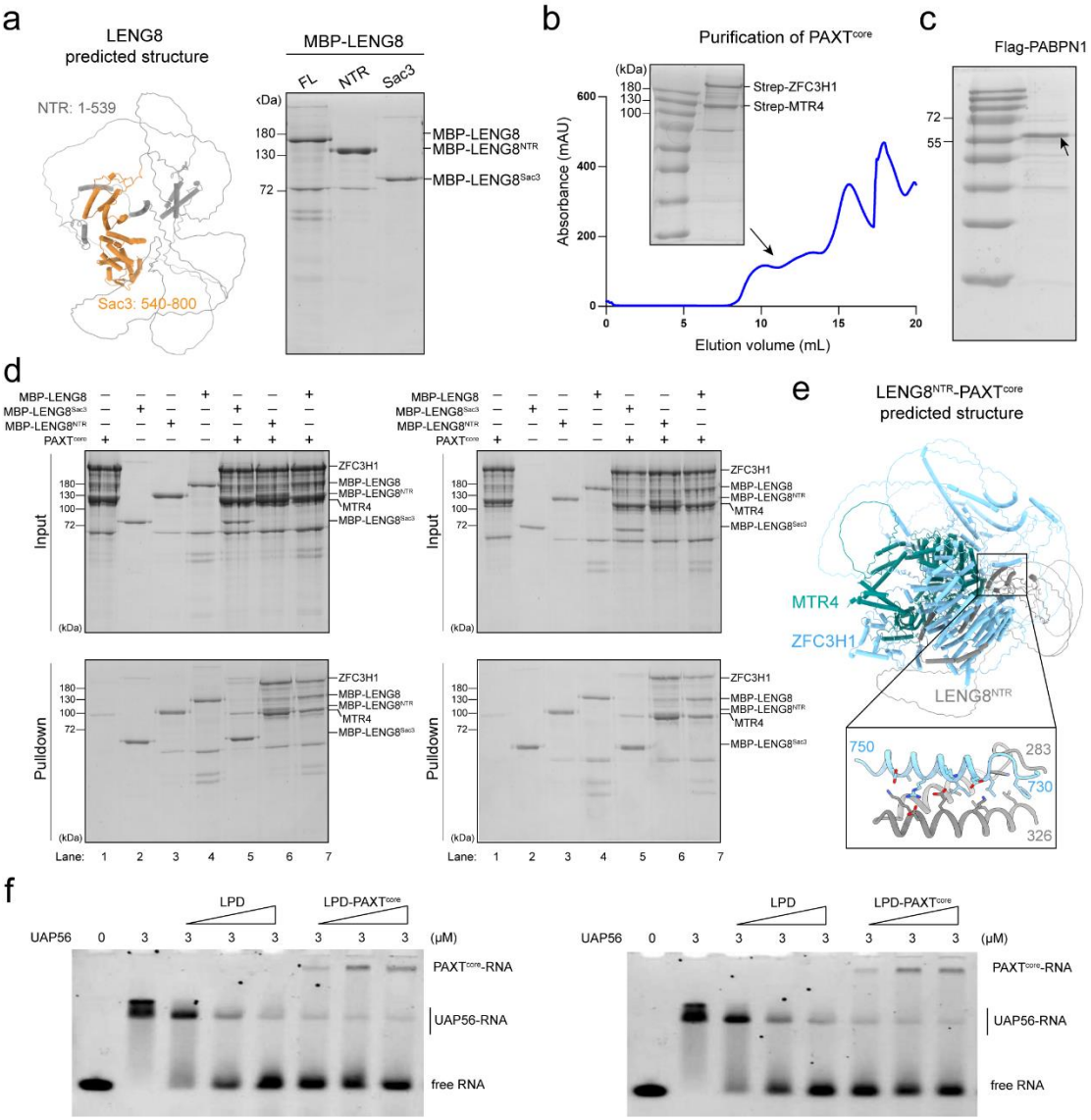

Supplementary Fig. 7 | Biochemical characterization of the LENG8-PAXT interaction and RNA transfer

a, Predicted structure of full-length LENG8 (left panel) and Coomassie blue-stained SDS-PAGE analysis of purified MBP-tagged full-length LENG8, LENG8^{NTR}, and LENG8^{Sac3} (right panel). **b**, Size-exclusion chromatography profile and SDS-PAGE analysis of the purified PAXT^{core} complex containing full-length ZFC3H1 and MTR4. **c**, Coomassie blue-stained SDS-PAGE analysis of purified Flag-PABPN1. The arrow indicates the PABPN1 band. **d**, Two independent MBP pulldown assays examining the interactions of full-length LENG8, LENG8^{NTR}, and LENG8^{Sac3} with the PAXT^{core} complex. Input and pulldown fractions were analyzed by SDS-PAGE. **e**, Predicted structure of the LENG8^{NTR}- PAXT^{core} complex. ZFC3H1, MTR4, and LENG8^{NTR} are

colored as indicated. The inset shows a close-up view of the predicted interface between ZFC3H1 and LENG8. **f**, Two independent native gel assays of the reconstituted RNA-release and RNA-capture reaction. Increasing concentrations of LPD promoted RNA release from preassembled UAP56-RNA complexes. In the presence of the $PAXT^{core}$ complex, the released RNA was incorporated into a slower-migrating $PAXT^{core}$-RNA complex.

Supplementary table 1 | Cryo-EM data collection, refinement and validation statistics

	URH49-SPD (EMDB-81691) (PDB 28ER)	**UAP56-SPD** (EMDB-81705) (PDB 28FK)	**UAP56-LPD** (EMDB-81704) (PDB 28FJ)
Data collection and processing			
Magnification	105,000×	105,000×	105,000×
Voltage (kV)	300	300	300
Electron exposure (e–/Å^2)	50	50	50
Defocus range (μm)	1.5~2.3	1.5~2.3	1.5~2.3
Pixel size (Å)	0.92	0.971	0.92
Symmetry imposed	C1	C1	C1
Initial particle images (no.)	2,298,323	785,269	1,013,869
Final particle images (no.)	249,215	272,959	268,320
Map resolution (Å)	3.07	3.08	3.13
FSC threshold	0.143	0.143	0.143
Map resolution range (Å)	2.8-3.8	2.7-4.0	2.7-3.8
Refinement			
Model resolution (Å)	3.2	3.3	3.3
FSC threshold	0.5	0.5	0.5
Map sharpening *B* factor (Å^2)	-88.3	-119.0	-100.0
Model composition			
Non-hydrogen atoms	9592	9318	7471
Protein residues	1184	1146	922
Ligands	2	2	1
B factors (Å^2)			
Protein	71.50	55.68	96.02
Ligand	72.16	35.53	110.60
R.m.s. deviations			
Bond lengths (Å)	0.003	0.004	0.003
Bond angles (°)	0.497	0.585	0.478
Validation			
MolProbity score	1.65	1.24	1.44
Clashscore	6.64	2.15	7.18
Poor rotamers (%)	0.10	0.20	0.00
Ramachandran plot			
Favored (%)	95.91	96.30	97.81
Allowed (%)	4.09	3.70	2.19
Disallowed (%)	0.00	0.00	0.00